A transported probability density function/photon Monte Carlo method for high-temperature oxy–natural gas combustion with spectral gas and wall radiation

X. Y. Zhao [a] [b] , D. C. Haworth [a] [b] , T. Ren [c] & M. F. Modest [c]

[a] National Energy Technology Laboratory – Regional , University Alliance (NETL-RUA)

[b] Department of Mechanical and Nuclear Engineering , Pennsylvania State University , University Park , PA , 16802 , USA

[c] Department of Mechanical and Applied Mechanics , University of California , Merced , CA , 95343 , USA
Published online: 14 Mar 2013.

PLEASE SCROLL DOWN FOR ARTICLE

Taylor & Francis
Taylor & Francis Group

A transported probability density function/photon Monte Carlo method for high-temperature oxy–natural gas combustion with spectral gas and wall radiation

X.Y. Zhao[a,b]*, D.C. Haworth[a,b], T. Ren[c] and M.F. Modest[c]

[a]*National Energy Technology Laboratory – Regional University Alliance (NETL-RUA);*
[b]*Department of Mechanical and Nuclear Engineering, Pennsylvania State University, University Park, PA 16802, USA;* [c]*Department of Mechanical and Applied Mechanics, University of California, Merced, CA 95343, USA*

A computational fluid dynamics model for high-temperature oxy–natural gas combustion is developed and exercised. The model features detailed gas-phase chemistry and radiation treatments (a photon Monte Carlo method with line-by-line spectral resolution for gas and wall radiation – PMC/LBL) and a transported probability density function (PDF) method to account for turbulent fluctuations in composition and temperature. The model is first validated for a 0.8 MW oxy–natural gas furnace, and the level of agreement between model and experiment is found to be at least as good as any that has been published earlier. Next, simulations are performed with systematic model variations to provide insight into the roles of individual physical processes and their interplay in high-temperature oxy–fuel combustion. This includes variations in the chemical mechanism and the radiation model, and comparisons of results obtained with versus without the PDF method to isolate and quantify the effects of turbulence–chemistry interactions and turbulence–radiation interactions. In this combustion environment, it is found to be important to account for the interconversion of CO and CO_2, and radiation plays a dominant role. The PMC/LBL model allows the effects of molecular gas radiation and wall radiation to be clearly separated and quantified. Radiation and chemistry are tightly coupled through the temperature, and correct temperature prediction is required for correct prediction of the CO/CO_2 ratio. Turbulence–chemistry interactions influence the computed flame structure and mean CO levels. Strong local effects of turbulence–radiation interactions are found in the flame, but the net influence of TRI on computed mean temperature and species profiles is small. The ultimate goal of this research is to simulate high-temperature oxy–coal combustion, where accurate treatments of chemistry, radiation and turbulence–chemistry–particle–radiation interactions will be even more important.

Keywords: oxy–fuel combustion; non-premixed turbulent flames; probability density function method; photon Monte Carlo method; high-temperature combustion

1. Introduction

Electricity generation and heating were responsible for 41% of 2009 global CO_2 emissions [1]. These applications rely heavily on coal, a carbon-intensive fossil fuel. Available near-term strategies to reduce CO_2 emissions from coal-firedpower plants include

---

*Corresponding author. Email: xzz105@psu.edu

pre-combustion capture, post-combustion capture and oxy–fuel combustion [2]. Oxy–fuel potentially could be implemented by retrofitting existing plants. In oxy–fuel combustion, a mixture of oxygen and recycled flue gas replaces air as the oxidiser to produce products that contain a high concentration of CO_2, which facilitates the separation of CO_2 from the other constituents. Flue-gas recirculation is usually used to maintain peak temperatures and heat-transfer rates that are comparable to those in a conventional air–fuel combustion system, thus minimizing combustor design changes. However, this approach gives up the efficiency benefit that potentially could be realised by taking advantage of the higher temperature of burning with oxygen instead of air. Direct power extraction using magnetohydrodynamics (MHD) has been proposed to take advantage of high combustion temperatures [3]. The concept of using an MHD topping cycle in a coal-fired power plant is not new, but it is being revisited in light of developments over the past 20 years that have addressed key issues [4]. One important area of development has been in advanced computational models for key physical processes and their interactions.

The overall goal of this research is to develop advanced computational fluid dynamics (CFD)-based models for turbulent combustion and heat transfer in high-temperature oxy–coal systems. The oxy–coal combustion environment differs from that in a conventional air–coal combustor in two important ways: higher temperatures (as high as $\sim 3000\,\mathrm{K}$), and higher concentrations of radiatively participating species (especially CO_2 and H_2O), in addition to coal particles and soot. These differences change the heat-transfer characteristics, thermodynamic and transport properties, gas-phase chemistry, and the devolatilisation, ignition and char burning rates for coal [2] compared to air-based combustion. The differences can be dramatic, and pose challenges for both computational models and experimental measurements. For example, heat transfer changes from being convection-dominated to radiation-dominated [5]; the importance of accurate radiation modelling is amplified. Chemical mechanisms that have been developed for air-based combustion need to be revisited and validated. Turbulent fluctuations in composition and temperature, and complex interactions among turbulence, gas-phase chemistry, solid particles, and radiation are expected to be especially important in oxy–fuel combustion [6].

For these reasons, a transported composition probability density function (PDF) method has been adopted as the basis for turbulent combustion modelling. This is coupled with a stochastic photon Monte Carlo (PMC) method for radiative heat transfer that maintains essentially line-by-line spectral accuracy [7]. PDF methods have proved to be particularly effective for dealing with turbulence–chemistry interactions in flames [8–10]. The coupled PDF/PMC model accounts for gas-phase turbulence–radiation interactions, and, when combined with a soot model (or models for other solid-phase particles, such as coal), for turbulence–particle–radiation interactions, in both Reynolds-averaged [11, 12] and large-eddy simulations [13]. For exploration of new combustion regimes such as high-temperature oxy–fuel, the coupled PDF/PMC model is expected to be advantageous compared to simpler models that require more flow-, chemistry- and radiation-specific tuning. This 'high-fidelity' model can be used to generate physical insight and to establish priorities for developing reduced models, should those be desired for computational expediency.

A systematic approach is being pursued for model development. First, simulations were performed for laboratory syngas ($CO/H_2/N_2$)–air non-premixed turbulent jet flames where detailed experimental measurements are available [14]. There the PDF/PMC models were implemented and tested in a combustion environment that is closer (compared to a conventional hydrocarbon–air flame) in product composition to that encountered in an oxy–fuel system. Excellent agreement with experiment was realised for syngas flames. Differences in chemical kinetics compared to hydrocarbon–air flames were pointed out,

and the importance of turbulence–chemistry interactions was demonstrated [15]. The next step (reported here) is to simulate an oxy–natural gas system where the environment is as close as possible to that in a high-temperature oxy–coal system, without the complications of a solid fuel. Key criteria for selecting the experimental configuration included the absence of flue-gas recirculation and wall cooling (to maintain high temperatures), and the availability of high-quality temperature and other measurements. For this purpose, a 0.8 MW oxy–natural gas burner was selected [16, 17]. Available experimental data include profiles of mean velocity, temperature and major species. Compared to early modelling studies of laboratory-scale open flames, the radiation modelling needs to be enhanced to account for emission and absorption by hot walls, and the radiation property database needs to be extended to higher temperatures. Chemical mechanisms that have been developed for air-based combustion need to be re-evaluated for the higher temperatures and different mixture compositions. And numerical algorithms have to be modified to deal efficiently with a relatively large-scale, closed device with complex internal flow structure. These issues and others are addressed in this article.

The remainder of the paper is organised as follows. In the next section, the target flame configuration is introduced and findings from earlier modelling studies are summarised. The physical models and numerical methods are described next. Then comparisons with experimental measurements and sensitivities to variations in model parameters are reported. In the final section, key findings are summarised and the next steps are outlined.

2. The OXYFLAM-2A oxy–natural gas flame

The target flame is one that was developed under the OXYFLAM project, supported by a consortium including the International Flame Research Foundation [16, 17]. The purpose of the project was to address the scarcity of comprehensive experimental data available for semi-industrial and full-scale combustion systems, towards developing a better understanding of oxy–fuel combustion. Results were reported for several configurations, including variations in burner geometry and inlet oxygen level. Here the second trial (a coaxial non-premixed jet flame issuing into a refractory-lined furnace) using 'burner A' has been selected, as this combination resulted in the highest peak temperature of approximately 3000 K. Detailed descriptions of the OXYFLAM-2A burner can be found in [16, 17]. This is a 0.8 MW, square-cross-section burner (1.05 m × 1.05 m) of 3.44 m length operating at an overpressure of 20 to 30 Pa. The fuel (natural gas) enters through a circular pipe at the centre of one end of the burner, and the oxidiser (oxygen) enters through an annular pipe that surrounds the fuel jet; combustion products exit at the opposite end through a 0.5 m diameter outlet. Key inlet parameters are listed in Table 1, and a sketch is provided in Figure 1. It was reported that the flame is essentially non-sooting, and no soot was collected in the experiments.

Several groups have published Reynolds-averaged CFD modelling studies for the OXYFLAM-2A flame. A summary of the codes and models that have been used is provided in Table 2. In most cases cited there, a two-dimensional (axisymmetric) computational domain was simulated and a two-equation k–ε turbulence model was used; in some cases, the value of $C_{\varepsilon 1}$ in the modelled dissipation-rate equation was changed from its standard value (Section 3.2). A variety of chemical mechanisms, turbulence–chemistry interaction (TCI) models, and radiation models has been used. General findings from earlier modelling studies are summarised as follows. It is important to account for high-temperature dissociation. Reduced mechanisms that were designed for air–natural gas combustion, such as the Westbrook and Dryer (WD) two-step mechanisms [18] and the Jones and Lindstedt (JL) four-step mechanisms [19], require modifications to account for the conversion of CO_2 to CO at high

Table 1. Inlet parameters for OXYFLAM-2A. In the experiment, the fuel was natural gas.

	Fuel jet	Oxidiser jet
Diameter (mm)	16	Inner $= 28$; outer $= 36$
Temperature (K)	300	300
Bulk velocity (m s^{-1})	105.4	109.7
CH$_4$ (mole fraction)	1	0
O$_2$ (mole fraction)	0	1
k (m^2 s^{-2})	628	850
ε (m^2 s^{-3})	4.6×10^6	2.9×10^6

Note: Wall temperature $T(x) = 1700.6 + 212.59x - 46.669x^2$ (K), where x is the axial distance from the burner in metres.

temperature [20, 21]. The accuracy of the CO and CO$_2$ predictions depends strongly on the chemical mechanism and on TCI. Several TCI models have been used, including an eddy-breakup (EBU) model, an eddy-dissipation concept (EDC) model, a presumed PDF model, a flamelet model, and a conditional moment closure (CMC) model [22]. However, no clear conclusions were drawn regarding the importance of TCI, as no systematic

(a) Geometry details.

(b) Mesh coloured by computed mean temperature contour.

(c) Zoomed-in mesh inside the flame zone.
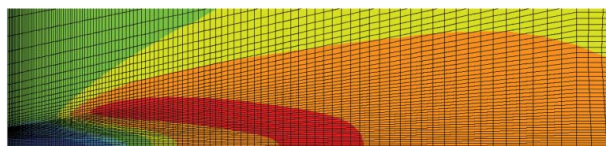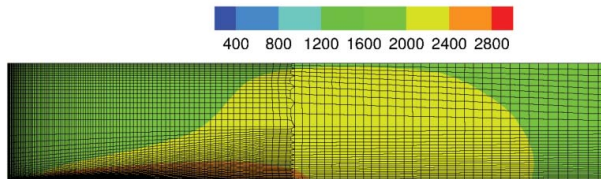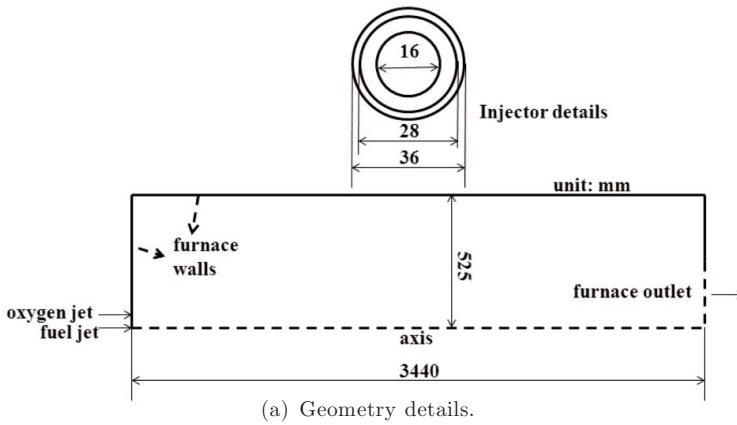
Figure 1. 2D sketch of the OXYFLAM-2A furnace, with inlet nozzle and mesh details.

Table 2.   Previous OXYFLAM-2A simulations.

Reference	Code	Turbulence	Turbulence–chemistry interaction	Chemical mechanism	Radiation
Breussin *et al.* [23]	Fluent 4.4 with NO$_x$ post-processor	Standard k–ε	EBU, EDC	Two-step reaction used with EBU; full equilibrium used with EDC	Discrete transfer method with constant absorption coefficient 0.3 m^{-1}
Brink *et al.* [24]	Fluent with user-defined EDC	Standard k–ε	Presumed PDF, EDC	Eight-species and eleven-species mechanisms	Discrete transfer method with constant absorption coefficient 0.3 m^{-1}
Kim *et al.* [25]	In-house code	Modified k–ε with $C_{\varepsilon 1} = 1.48$	Non-adiabatic flamelet	GRI-Mech 2.11	Finite volume method with constant absorption coefficient 0.3 m^{-1}
Kim *et al.* [26]	In-house code	Modified k–ε with $C_{\varepsilon 1} = 1.50$	CMC	GRI-Mech 2.11	Finite volume method with constant absorption coefficient 0.3 m^{-1}
Yin *et al.* [20]	Ansys Fluent 12.1	Standard k–ε	ED	WD, refined WD, JL, refined JL	Discrete ordinates method with modified WSGGM

comparisons were made among different TCI treatments. Both grey gas [23–26] and non-grey gas [20] radiation properties have been used in the radiation models (WSGGM denotes a weighted sum of grey gases model), but no systematic comparisons have been made between results obtained with different radiation models, or to quantify the importance of radiation (e.g., by comparing results obtained with versus without a radiation model). It was noted that the specification of the wall temperature is important for correctly predicting the flame temperature [25]; in all of the studies cited in Table 2, the experimentally measured wall-temperature profile was imposed as a boundary condition (Table 1). In addition to uncertainties arising from the computational models, uncertainties in the experimental data have been mentioned as a potential source of discrepancy between computations and experiment, especially at the high temperatures that are encountered in this system (Section 4.1). The geometric simplification of axisymmetry is expected to contribute to differences between model and experiment in the large, slow recirculation zones outside of the main combustion zone. And while it has been argued that turbulence–chemistry and turbulence–radiation interactions should be important in this environment [6], these effects have not been quantified.

Here, detailed chemistry and radiation treatments are implemented in a framework that allows the influences of turbulent fluctuations and turbulence–radiation interactions to be

captured accurately. Simulations are performed with systematic variations in key models to provide insight into the roles of individual physical processes and their interplay in high-temperature oxy–fuel combustion environments. In this manner, the relative importance of different physical processes is isolated and quantified, and this provides guidance for the development of simpler models that can be used for more routine engineering analysis and design.

3. Physical models and numerical methods

A consistent hybrid Lagrangian particle/Eulerian mesh method is used to solve a modelled transport equation for the joint PDF of species mass fractions and mixture specific enthalpy in a Reynolds-averaged formulation. A photon Monte Carlo (PMC) method with line-by-line (LBL) spectral accuracy is used to solve the radiative transfer equation. The physical models and numerical methods are introduced in subsequent subsections. Further information about the PDF method can be found in [9], and details of the PMC/LBL method can be found in [7, 27–29].

3.1. *Thermochemical properties and chemical mechanisms*

A reacting ideal-gas mixture is considered. Accurate treatment of CO/CO_2 interconversion is especially important in oxy–fuel combustion [30, 31]. Highly reduced hydrocarbon–air mechanisms (e.g., [18, 19]) that are currently employed in most industrial CFD calculations cannot be expected to capture the chemical effects of high CO_2 levels in oxy–fuel combustion, due to their simplified description of the CO/CO_2 conversion rate [30].

Here, results obtained using three different chemical mechanisms are compared to elucidate chemical effects in this combustion environment: GRI-Mech 2.11 [32] (49 species), a 21-species C1 mechanism [33], and a 16-species skeletal methane–air mechanism [34]. All three mechanisms have been used in turbulent air–fuel combustion simulations (e.g., [15, 35]). GRI-Mech 2.11 was developed specifically for natural-gas combustion, and includes C2 chemistry. However, neither GRI-Mech 2.11 nor the 16-species skeletal mechanism were originally intended for the high-temperature oxy–fuel combustion environments that are of interest here. GRI-Mech 2.11 has been used for simulations of the OXYFLAM-2A furnace in [25, 26], and reasonably good results were obtained compared to experiment.

All three mechanisms include the reaction $CO_2 + H \rightleftharpoons CO + OH$, which is expected to be the primary path responsible for the chemical effects of CO_2. Reactions with methylene are also found to be important for the consumption of CO_2, but methylene is usually present in small concentrations in oxygen–natural gas combustion. Of the three mechanisms, GRI-Mech 2.11 includes methylene reactions and has the most comprehensive CO_2-related chemistry, while the 16-species mechanism has the least. In some cases, the rate coefficients for key elementary reactions are different in the three mechanisms. For example, the 21-species C1 mechanism has been updated recently [33] with new rate coefficients for the key reactions $CO_2 + H \rightleftharpoons CO + OH$ and $HCO + M \rightleftharpoons H + CO + M$; the model also uses a modified heat of formation for the OH radical. These changes are expected to have a significant influence on CO and temperature prediction [33].

The 16-species and 21-species mechanisms are provided in the Supplemental Material for reference, while GRI-Mech 2.11 can be found in [32]. GRI-Mech 2.11 has been adopted as the baseline mechanism for this study.

3.2. *Hybrid Lagrangian particle/Eulerian mesh PDF method*

The $N_S + 1$ composition variables are taken to be the mass fractions of the N_S species Y in the chemical mechanism, plus the mixture-specific absolute enthalpy h (the sum of the sensible and formation enthalpies). These are sufficient to determine the local temperature T, mixture mass density ρ, chemical source terms S_{reac}, spectral absorption coefficient κ_η, Planck function $I_{b\eta}$, and any other thermodynamic or transport properties that are needed. The sample-space vector corresponding to the $N_S + 1$ composition variables is denoted as $\boldsymbol{\psi}$. Then the PDF transport equation, expressed as an equation for the composition mass density function $\mathcal{F} = \mathcal{F}(\boldsymbol{\psi}; \boldsymbol{x}, t)$, can be written as

$$\frac{\partial \mathcal{F}}{\partial t} + \frac{\partial}{\partial x_i}[\tilde{u}_i \mathcal{F}] + \frac{\partial}{\partial \psi_\alpha}[S_{\alpha,\text{reac}}(\boldsymbol{\psi})\mathcal{F}] - \delta_{\alpha h} \frac{\partial}{\partial \psi_\alpha}\left[\rho^{-1}(\boldsymbol{\psi})\mathcal{F} \, 4\pi \int_0^\infty \kappa_\eta(\boldsymbol{\psi}) I_{b\eta}(\boldsymbol{\psi}) \, \mathrm{d}\eta\right]$$

$$= -\frac{\partial}{\partial x_i}[\langle u_i'' | \boldsymbol{\psi}\rangle \mathcal{F}] + \frac{\partial}{\partial \psi_\alpha}\left[\left\langle \rho^{-1}(\boldsymbol{\psi})\frac{\partial J_i^\alpha}{\partial x_i} | \boldsymbol{\psi}\right\rangle \mathcal{F}\right] - \delta_{\alpha h} \frac{\partial}{\partial \psi_\alpha}\left[\left\langle \rho^{-1}(\boldsymbol{\psi}) \int_0^\infty \kappa_\eta(\boldsymbol{\psi}) G_\eta \, \mathrm{d}\eta | \boldsymbol{\psi}\right\rangle \mathcal{F}\right].$$

(1)

Here, $\boldsymbol{u}$ is the velocity vector, $\boldsymbol{J}^\alpha$ is the molecular flux vector of composition variable α, and G_η is the spectral incident radiation (the direction-integrated radiative intensity, I_η). A Roman subscript denotes a physical-space coordinate ($i = 1, 2, 3$), a Greek subscript denotes a composition-space coordinate ($\alpha = 1, 2, \ldots, N_S, N_S + 1$), summation is implied over a repeated Roman or Greek index within a term, and $\delta_{\alpha h}$ denotes the Kronecker delta function ($\delta_{\alpha h} = 1$ for $\alpha = N_S + 1$ corresponding to enthalpy h; $\delta_{\alpha h} = 0$ otherwise). Variables in angled brackets are mean values, the notation $\langle A|B\rangle$ denotes the conditional mean of event A given that event B occurs, and variables with tildes and double primes are Favre-averaged mean values and fluctuations with respect to the local Favre-averaged mean value, respectively. Terms on the left-hand side of Equation (1) (time-rate-of change, convection by the mean velocity, chemical reaction and radiative emission) are in closed form, while terms on the right-hand side need to be modelled.

The first term on the right-hand side represents transport in physical space due to turbulent velocity fluctuations, which is modelled using a gradient transport model. The second term represents transport in composition space by molecular transport (mixing), which is modelled using the Euclidean minimum spanning tree (EMST) mixing model [36]. The last term on the right-hand side corresponds to radiative absorption, which is modelled as described in Section 3.3. The selection of EMST as the baseline mixing model is consistent with the philosophy of using the best available models for each physical process. For these flames, the results are essentially the same with simpler mixing models (Section 4.4.3). Computational cost for the mixing model is negligible compared to that for chemistry and radiation.

A consistent hybrid particle-mesh method is used to solve the modelled composition PDF equation. The coupled mean velocity, mean pressure and turbulence model equations are solved using an unstructured finite-volume method with second-order spatial discretisations and first-order time discretisation using a PISO-based, time-implicit segregated solver that has been built using elements from OpenFOAM-1.5 [37]. Here, a standard two-equation k–ε turbulence model is used, including wall functions. The principal governing equations on the finite-volume side can be found in Sections 4.3 and 6.1 of [9], for example. A Lagrangian particle Monte Carlo method is used to solve the modelled composition PDF equation, by introducing a system of notional particles [8]. Species mass fractions and mixture specific enthalpy are computed using the notional particles, and local mean scalar values are estimated as appropriately weighted averages over particle values.

The apparent turbulent diffusivity and the turbulent mixing frequency that are needed in the models for turbulent transport and molecular transport, respectively, are calculated using the turbulence kinetic energy k and the viscous dissipation rate of turbulence kinetic energy ε. The principal feedback from the particle side to the finite-volume side of the calculation is through the mean density; this is handled using an equivalent-enthalpy-based approach [38, 39]. Details can be found in Section 7.1 of [9]. Steady-state solutions are obtained by marching in time until a statistically stationary state is reached.

Starting from quiescent initial conditions, the physical time required to reach steady state is quite long compared to that for an open jet flame, for example. In particular, a large number of flow-through times is required to establish the slow, large-scale recirculation zones outside of the relatively compact turbulent flame (Section 4.1). To reduce the computational time required, the 'tightly coupled' particle-mesh algorithm that has been used in most of our earlier modelling studies (particle side called on every finite-volume computational time step) was modified to a 'loosely coupled' algorithm [38]. In the loosely coupled algorithm, the finite-volume side is run for multiple time steps between calls to the particle solver with the mean values that are taken from the particle side held fixed; the particle side is then advanced for multiple time steps with the mean values that are taken from the finite-volume side held fixed; and this is repeated until a converged steady-state solution is obtained.

Standard values have been used for all model coefficients, with the exception of the mixing model constant C_ϕ (the ratio of a turbulence velocity time scale to a turbulence scalar mixing time scale). The values of C_ϕ that have been used by different investigators using different mixing models and for different flame configurations vary widely, although the reported variation has been somewhat less for EMST compared to simpler mixing models [35]. Based on matching computed and measured profiles of mean temperature, the value $C_\phi = 5.5$ has been adopted here for the baseline model; this is higher than the value of 1.5 that worked well for a series of piloted non-premixed turbulent methane–air flames, for example [35]. It is not clear why a higher value of C_ϕ appears to be appropriate here. The aero-thermo-chemical conditions are quite different from those in earlier PDF-based modelling studies. Also, the turbulence is intense only in a relatively compact flame zone, whereas both the flame zone and the outer recirculation zone influence the mean temperature and composition fields. Mixing models remain a key outstanding issue in PDF methods [10]. The influence of a variation in the value of C_ϕ on computed mean profiles is explored in Section 4. As shown there, it is not clear that $C_\phi = 5.5$ is necessarily the best value for this flame.

Another coefficient that is often adjusted in modelling studies (with or without a PDF method) of round jets is the k–ε model coefficient $C_{\varepsilon 1}$ in the modelled ε equation. Increasing the value of $C_{\varepsilon 1}$ from its standard value of 1.44 increases the jet penetration and decreases the spread rate, and generally is found to give better agreement with experiment for free turbulent round jets and jet flames [15, 35]. It has also been found to improve results for the confined flame that is the subject of the current modelling study [25, 26]. Here, the standard value ($C_{\varepsilon 1} = 1.44$) has been adopted for the baseline model, and the effects of increasing $C_{\varepsilon 1}$ to a value of 1.56 are explored in Section 4. Baseline physical models and numerical parameters are summarised in Table 3.

3.3. *Radiative heat transfer*

Radiation plays an important role because of the large furnace volume, the high flame temperature, the high concentrations of participating species and the hot refractory walls. For a participating medium, the local radiative intensity is obtained by solving the radiative

Table 3. Baseline physical models and numerical parameters.

Item	Model	Model parameters	Baseline values
Eulerian CFD	Unstructured finite-volume method	Mesh size and distribution	Axisymmetric 10,260 cells (Figure 1)
Turbulence closure	k–ε	C_μ, $C_{\varepsilon 1}$, $C_{\varepsilon 2}$, σ_k, σ_ε	$C_\mu = 0.09$, $C_{\varepsilon 1} = 1.44$, $C_{\varepsilon 2} = 1.92$, $\sigma_k = 1.0$, $\sigma_\varepsilon = 1.3$
Wall turbulence	Standard wall function	κ, E	$\kappa = 0.4187$, $E = 9.8$
TCI closure	Composition PDF method	Number of notional particles (+ turbulent and molecular flux models)	Thirty particles per cell
Turbulent fluxes	Gradient transport	Turbulent Schmidt (Sc_T) and Prandtl (Pr_T) numbers	$Sc_T = Pr_T = 1$
Molecular mixing	EMST model	C_ϕ	$C_\phi = 5.5$
Gas-phase chemistry	GRI-Mech 2.11	—	—
Gas-phase radiative properties	Line-by-line databases	Database, number of participating species	(HITEMP2010): H_2O, CO_2, CO to 3000 K
RTE solver	Full non-grey photon Monte Carlo	Numbers of photon bundles traced per time step, ε_{wall}	One ray per PDF particle, $\varepsilon_{wall} = 0.7$
TRI closure	Emission and absorption TRI	Full TRI, emission TRI only, no TRI	Full TRI

transfer equation [40]. Here, a stochastic spectral photon Monte Carlo method is used for that purpose. Notional photon bundles are emitted by each PDF particle (Section 3.2) based on the particle's composition and temperature. No approximations are made regarding the directional or spatial dependence of intensity, and essentially line-by-line spectral resolution is maintained. Each photon bundle's wavenumber, direction and energy are sampled from distributions that correspond (in the limit of an infinite number of samples) to the correct local spectral rate of emission. Each PDF particle that is encountered along the photon bundle's trajectory absorbs energy based on the local absorption coefficient (determined by the particle's composition and temperature). The photon bundle is traced until its energy is depleted to zero, it encounters a wall, or it exits the computational domain. Because local emission and absorption rates are based on PDF particle values (rather than on finite-volume cell-mean values), emission and absorption turbulence–radiation interactions are fully accounted for (Section 3.4). The PDF/PMC/LBL models are described more fully in [7, 27, 28]. Examples of their application in a Reynolds-averaged formulation can be found in [11, 12] and an example in large-eddy simulation can be found in [13, 29].

Compared to our earlier PDF/PMC/LBL modelling studies, there are three new elements to the radiation modelling here: CO emission/absorption has been added (in addition to CO_2 and H_2O) because of the high CO concentrations in the furnace; the radiation property database has been extended to temperatures up to 3000 K (from 2500 K in earlier work); and wall absorption/reflection and emission models have been implemented to accommodate

the hot walls (wall temperatures as high as 1940 K). The LBL spectral database updates were made using the HITEMP2010 database [41, 42].

In this furnace, a significant fraction of the radiation emitted by the gas is reabsorbed by the gas. Wall boundary conditions for radiation can be quite complicated, depending on the wall material and the environment. The radiative properties can vary appreciably across the spectrum, and surface absorptance and reflectance can depend on the direction of the incoming radiation and/or on temperature [40]. Detailed spectral and directional data are not available for the refractory material that was used in OXYFLAM-2A. Therefore, simplifications are made based on experience with similar materials in similar environments. The refractory walls are assumed to be grey and diffuse in both emission and reflection. Diffuse emission is nearly always acceptable, and it is usually sufficient to assume diffuse reflection for enclosures at all but extreme aspect ratios [40]. For coal furnaces, surfaces covered with ash deposits or slag can also be approximated as grey and diffuse at sufficiently high temperatures (above 1400 K). At lower temperatures, the radiation properties of an ash-covered wall can be both temperature- and wavelength-dependent [43]. Since a high-temperature environment is of interest here, a grey and diffuse wall assumption should be sufficient both for the current configuration (without ash or slag) and for future simulations of coal combustion. Here a constant wall emissivity of 0.7 is assumed [23]. In the PMC model, a fraction of the energy of each photon bundle that reaches a wall is absorbed by the wall; the remaining energy is reflected diffusely (i.e., in a random direction) back into the furnace from the intersection point with the wall. Wall emission is handled by diffuse emission of new photon bundles with wavelengths corresponding to a grey body at the local wall temperature and with the total emitted energy corresponding to the (here constant) emissivity. Because the gas absorbs only in discrete wavenumber bands, it is essentially transparent to the emitted wall radiation. Therefore, most photon bundles that correspond to wall emission will reach another wall, where they in turn will be absorbed or reflected. Wall-emission photon bundles can traverse the computational domain many times before their energy is finally depleted or they exit the computational domain. For this reason, the PMC/LBL radiation calculation is computationally intensive, and is dominated by the tracing of photon bundles.

In most earlier modelling studies (Table 2), a constant global absorption coefficient has been assumed [16, 25, 26]. In general, it is expected that net emission will be underestimated by a grey model, and that the computed temperatures will be correspondingly higher, because no distinction is made between the wavenumbers at which the gas emits/absorbs and those at which the walls emit/absorb.

3.4. *Turbulence–chemistry interactions and turbulence–radiation interactions*

The most compelling reason for bringing a coupled PDF/PMC method to bear in turbulent oxy–fuel combustion is its advantages in dealing with the effects of unresolved turbulent fluctuations in composition and temperature. In the hybrid particle/mesh formulation, for example, the finite-volume cell-level mean chemical and radiation source terms computed based on particle values of composition and temperature in general can be very different from those computed based on cell-mean values of composition and temperature; the differences are manifestations of 'turbulence–chemistry interactions' (TCI) and 'turbulence–radiation interactions' (TRI), respectively. These differences arise because the chemical and radiation source terms are nonlinear functions of composition and temperature. With the coupled PDF/PMC method, complex turbulence–radiation interactions are captured accurately, and this has been amply demonstrated in earlier modelling studies of

open flames [11–13, 29]. It has been suggested that these interactions may be especially important in oxy–fuel combustion environments [6]. In the PDF/PMC method, the effects of TCI and TRI can be isolated and quantified to establish their relative importance. For example, TCI can be quantified by comparing results obtained by computing the chemical source terms based on finite-volume cell-mean values of composition and temperature (thereby neglecting the effects of turbulent fluctuations on reaction chemistry – a well-stirred-reactor model at the finite-volume cell level) and comparing with results obtained by computing the chemical source terms based on particle values (thereby capturing the effects of turbulent fluctuations). Similarly, TRI effects can be quantified by computed radiation based on cell-mean values of composition and temperature and comparing the results with those obtained by computing radiation based on particle values; this can be done separately for emission and for absorption to further elucidate how the effects of fluctuations are manifested [13, 29]. Results from exercises of this kind are provided in Section 4.

3.5. *Computational mesh, initial and boundary conditions*

As in earlier modelling studies [23–26], simulations are performed for a two-dimensional (axisymmetric) domain, for computational expediency. The computational domain is a 10-degree wedge with a single finite-volume cell in the azimuthal direction. It extends from the jet nozzle exit ($x = 0$) to the furnace outlet ($x = 3.44$ m) in the streamwise direction, and from the furnace centreline ($r = 0$) to the wall ($r = 0.525$ m) in the radial direction. The total volume is thus somewhat smaller than that in the actual furnace. In some of the earlier studies, a short outlet 'chimney' downstream of $x = 3.44$ m was included. It has been confirmed that the computed mean flow patterns do not change significantly when a 0.5 m long outlet chimney is added to the computational domain. These geometric approximations will influence the computed flow structure outside of the main reaction zone to some extent, but are expected to have limited influence on the turbulent flame structure or on the principal conclusions that are drawn from this study.

The baseline unstructured computational mesh of 10,260 finite-volume cells is non-uniformly distributed, with higher resolution in the mixing/reaction zone (small x and r). Sensitivity of computed results to variations in grid size and distribution has been explored by comparing results from the baseline mesh with those obtained using a uniform structured mesh of 8880 cells. While the total number of cells is similar for both meshes, the spatial distribution of resolution is quite different. The uniform structured mesh has similar resolution in the radial direction in the flame zone, and is finer by approximately a factor of two in the radial direction outside of the flame. In the axial direction, the uniform structured mesh is approximately 75% coarser than the baseline mesh. Differences in computed radial profiles of mean temperature and species profiles for the two meshes differ by no more than 5% at the axial measurement locations of primary interest ($x = 0.22$ m, $x = 0.82$ m and $x = 1.42$ m; not shown).

Based on results from earlier PDF modelling studies of statistically stationary flames (e.g., [35]), the nominal number of PDF particles per cell is set at $N_{PC} = 30$ and the particle number density is controlled using algorithms that are described in Section 7.1 of [9]. The number of photon bundles emitted and traced per computational time step by the gas is approximately equal to the number of PDF particles [29]. And based on the results of numerical experiments, the number of wall-emission photon bundles per time step is approximately 25% of the gas-emission photon bundles number. Relatively small numbers of samples are sufficient for statistically stationary systems, because time averaging can be

used to reduce statistical error. Top-hat inlet mean velocity and composition profiles are specified, based on the experimental measurements (Table 1). The inlet values of k and ε are specified in a manner that corresponds to a turbulence intensity of approximately 20% estimated from the measured axial mean and rms velocity at $x = 0.22$ m [17], and a turbulence integral length scale that is approximately 7% of the fuel-jet radius or 30% of the annulus gap. It has been observed from numerical experiments that the results are not sensitive to the specification of the length scales at the inlet. At the outlet, a fixed pressure of one atmosphere is specified and zero-gradient conditions are used for all other variables. No-slip wall boundary conditions are applied at the outer radial boundary and on the inlet and outlet planes that correspond to walls. A constant, non-uniform temperature boundary condition taken from the experimental data [20] is specified along the outer wall (Table 1), while zero-gradient boundary conditions are specified for the walls at the inlet and outlet planes since no temperature measurements were provided there. Symmetry conditions are applied on the azimuthal faces. The composition of the natural gas used in the experiments is given in [16]. Here, pure methane is used to facilitate comparisons of results from different chemical mechanisms, not all of which include hydrocarbons beyond C1. It has been confirmed that the mean profiles presented in Section 4 change by less than 10% when the actual fuel composition is considered. More discussions on the effect of fuel composition can be found in Section 4.1.

Starting from quiescent initial conditions, a steady-state solution is first obtained without the PDF method: i.e., using finite-volume cell-level mean temperatures and compositions directly in the chemical mechanism – a well-stirred-reactor (WSR) chemical model. This is then taken as the initial condition for the PDF solver. The PDF simulation is advanced using a computational time step of 10 μs (corresponding to a maximum material Courant number of approximately unity) until a statistically stationary state is reached: approximately 8 s in physical time, or 250 flow-through times based on the inlet jet velocity, or three flow-through times based on the large recirculation-zone residence time. Results are then time-averaged for approximately 0.5 s (corresponding to 15 flow-through times based on the inlet jet velocity) to reduce statistical noise in the reported mean and rms profiles.

3.6. *Computational acceleration*

Several strategies have been implemented to reduce the computational time required. These include the loosely coupled particle/finite-volume algorithm and the use of a WSR chemistry model to initialise the PDF simulations, as mentioned earlier. Two other techniques that have been used are *in situ* adaptive tabulation (ISAT) to accelerate the calculation of chemical source terms [44] and domain-decomposition-based parallelisation. The ISAT global error tolerance is taken to be 10^{-3}, a value that was found to be appropriate in earlier modelling studies of statistically stationary flames [9, 35]. Results obtained using ISAT have been compared with those obtained using direct integration of the chemical source terms for the baseline physical models, to confirm that the results presented below and the conclusions that are drawn from them are not influenced significantly by ISAT. The largest differences between ISAT and direct integration are in minor species profiles downstream in the combustor. In all cases, the maximum difference between ISAT and direct integration is less than 5% for all variables that are presented in Section 4 below, while the overall simulation time with ISAT is approximately 25% of that for direct integration. Here, mildly parallel runs have been performed using up to eight cores, and a simple domain decomposition scheme has been used in which the computational domain is split in the axial and/or radial directions (e.g., two in the radial direction and four in the axial direction) such

that each core has approximately the same number of cells. A speedup of approximately a factor of four is achieved on eight cores compared to a single core. As noted earlier, PMC ray tracing dominates the radiation computational effort. For a parallel run with ISAT and baseline models, the computational time required for radiation ray tracing is approximately twice that for mixing and chemistry combined, while the time spent in the finite-volume flow solver is negligible compared to chemistry or radiation.

4. Results and discussion

Results obtained using the baseline model (Table 3) are presented first and discussed. In the remaining three subsections, the effects of variations in key physical models are explored to provide deeper insight into high-temperature oxy–fuel combustion and guidance for modelling. All mean and rms profiles presented in this section correspond to mass-(Favre-) averaged values.

4.1. *Baseline model results and global flame characteristics*

Computed steady-state mean temperature and major-species mass-fraction contours with superimposed mean streamlines are shown in Figure 2. The maximum computed mean temperature is 2974.6 K, which is close to the adiabatic flame temperature of 3055.7 K. The computed flame length based on the measured CO equilibrium value (2.3% dry basis) is 234 cm, which is slightly shorter than the measured value of approximately 245 cm [16]. There is a large, slow (axial mean velocity magnitude approximately $1\,\mathrm{m\,s^{-1}}$) recirculation zone outside of the flame zone that fills most of the burner, and a smaller recirculation zone in the corner ($x = 0$, $r = 0.525$ m). The large recirculation zone is filled with a mixture of more than 90% CO_2 and H_2O at a temperature of approximately 2000 K. CO concentrations in the near-nozzle high-temperature region are higher than those in a conventional air–natural gas combustor, and this can have implications for near-burner corrosion and slagging [30]. However, CO emissions are not a serious concern, as the CO is converted to CO_2 downstream. Based on the global flame structure shown in Figure 2, the furnace can be divided into two regions with different characteristics. One is the high-temperature flame zone where the residence time is short, turbulence is intense, and finite-rate chemistry may be important; the other is the large recirculation zone where the residence time is long, turbulence is weak, the temperature remains relatively high, and near-equilibrium chemistry is expected. These two regions will be distinguished in subsequent discussions on radiation and turbulence-chemistry-radiation interactions.

Comparisons of computed and measured radial profiles of mean temperature, velocity and major species at three axial locations ($x = 0.22$ m, $x = 0.82$ m and $x = 1.42$ m) are shown in Figure 3. The axial mean velocity is underpredicted at all three locations. Mod-elling contributions to this discrepancy could include the top-hat inlet velocity profiles that have been prescribed, the simple turbulence model that has been used, and the geometric simplifications that have been invoked. Computations using a fully-developed turbulent mean velocity profile at the inlet show no significant differences (not shown). It may be that the geometry approximation that has been made (round versus square cross sections) alters the structure of the recirculation zone, and consequently the mean velocity profiles at downstream locations. Under-entrainment of cooled product gas into the hot flame zone in simulations has been discussed by Kim *et al.* [26]. The computed mean temperature profiles agree well with experiments in the recirculation zone (maximum difference of less than 100 K) and are higher than the measurements (locally by as much as 500 K) in the

(a) Mean temperature.

(b) Mean CO_2.

(c) Mean H_2O.

(d) Mean CO.
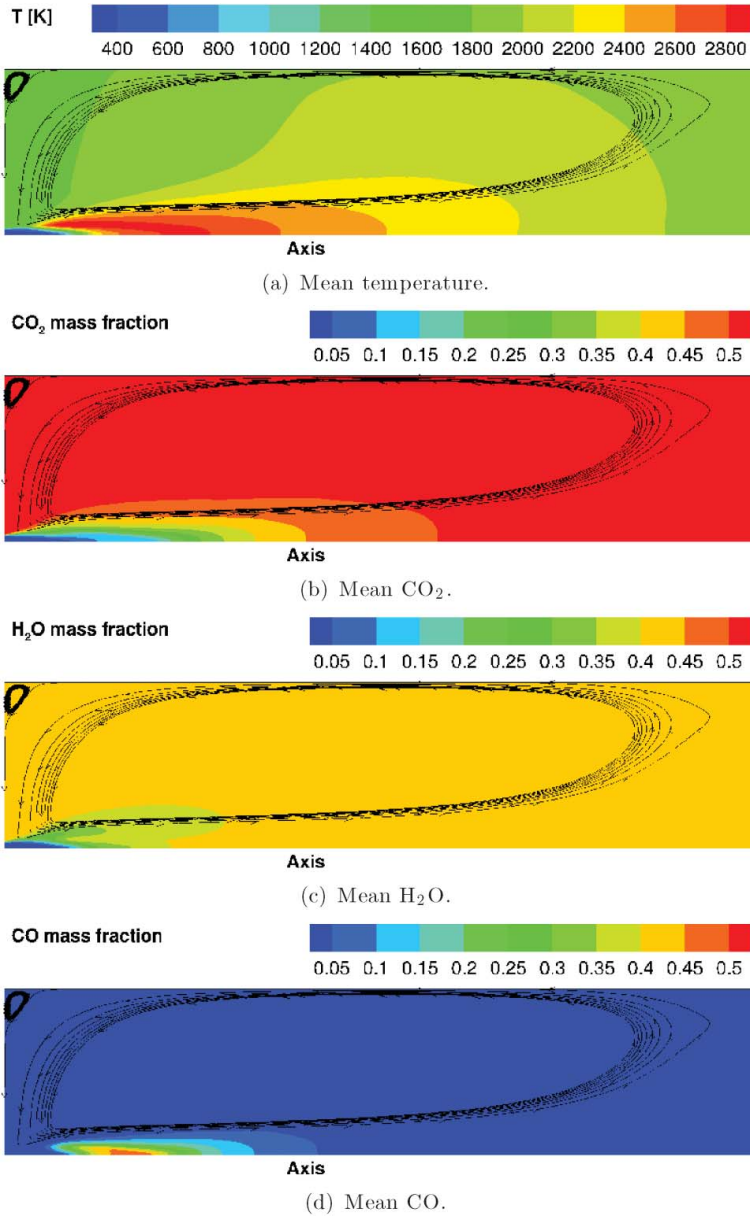
Figure 2. Computed (baseline model) mean temperature and major species contours, with mean streamlines.

core flame region. Experimental uncertainty is a particular concern for the temperature measurements [26]. An intrusive probe was used in the experiments, and the raw measured gas temperature is several hundred degrees lower than the true gas temperature due to cooling by the probe tip. The temperature data were corrected using CARS-based calibration curves that extend to 2400 K [17]. The reliability of the temperature measurement technique was evaluated using equilibrium calculations based on measured H_2 concentrations, and
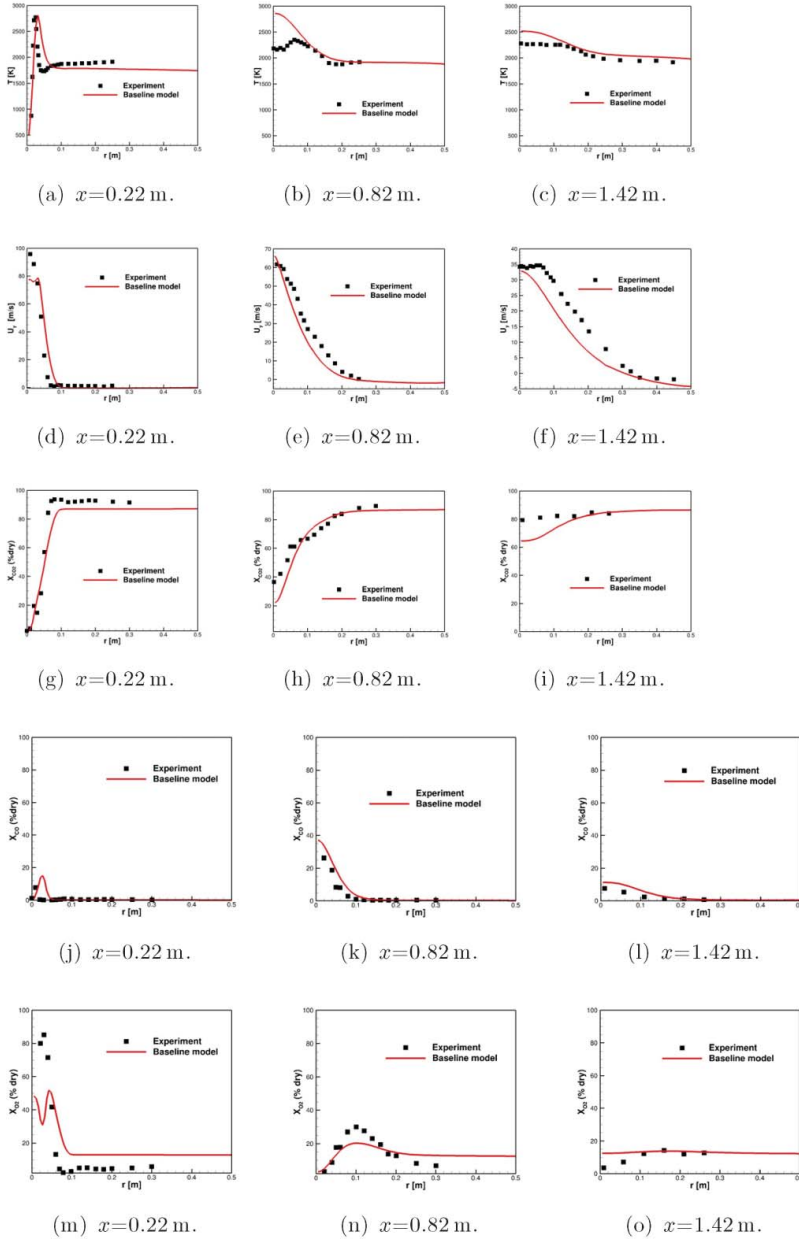
Figure 3.   Computed (baseline model) and measured radial profiles of mean temperature, axial velocity, CO_2, CO and O_2 (available in colour online).

it was shown that the measured temperature after CARS correction agreed well with the temperature deduced from the H_2-equilibrium calculation except for a higher temperature zone outside the flame core at upstream locations [25]. This suggested that experimental uncertainty in the temperature measurement could be high, especially in and near the hot flame zone [26]. On the modelling side, a temperature overprediction could result from an

underestimate of the degree of dissociation in the oxy–fuel environment, for example. As discussed in Section 3.1, the CO/CO_2 interconversion is especially important in oxy–fuel combustion. CO_2 is favoured at lower temperature [30], so the lower computed CO_2 and higher computed CO levels compared with experiment in the flame zone are consistent with the higher computed temperatures. Results from different chemical mechanisms (and their corresponding thermodynamic data) can be quite different, as will be shown in Section 4.3. There is some improvement in the computed O_2 and CO_2 profiles when the actual fuel gas composition is considered (not shown), which results mainly from the inclusion of CO_2 in the fuel and the higher carbon-to-hydrogen ratio in natural gas compared to methane. While some earlier modelling studies (Table 2) have reported somewhat better agreement with experiment for specific variables at specific spatial locations, the overall level of agreement between model and experiment here is at least as good as (or better than) any that has been published to date for this burner. Because of the large uncertainties in the temperature measurements in the high-temperature region, in particular, the emphasis in the following is on exploring the influences of variations in key submodels to generate physical insight, rather than on seeking better conformity between model and experiment. In particular, the high temperatures and high participating-species concentrations suggest that radiation heat transfer is important, and this is discussed next.

4.2. *Radiation*

As discussed earlier, wall radiation is important in this configuration, and wall reflection, absorption and emission are included in the model. Simpler wall radiation treatments (e.g., cold wall as in earlier open-flame simulations [15], or adiabatic wall) yield unrealistic temperatures in the recirculation zone (as much as 100 K higher for an adiabatic wall) compared to the more detailed treatment (not shown).

According to the model, during one computational step, approximately 82% of the total radiative energy E_{tot} is emitted by the gas-phase, and 18% is emitted by the wall. Seventy-five per cent of E_{tot} is absorbed by the gas-phase, and the remaining 25% is absorbed by walls or is lost through inlet/outlet boundaries. The re-aborption of gas-emitted energy is as high as 91%, and most of the wall-emitted energy is re-absorbed by walls or is lost through inlet/outlet. This is due to the different spectral characteristics of the grey wall and the spectral-dependent gas phase. It has been observed that tracing the wall-emitted photon bundles accounts for almost 55% of the total radiation calculation time. This computational inefficiency could be improved by the employment of wavenumber-selective ray-tracing schemes for the wall in the future.
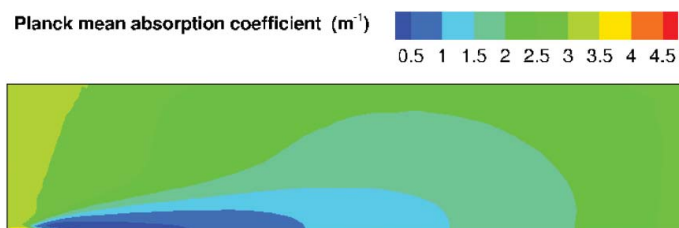
Figure 4.   Computed (baseline model) Planck mean absorption coefficient distribution (available in colour online).

Figure 4 shows the computed distribution of the Planck mean absorption coefficient κ_P based on finite-volume cell-level mean temperature, CO_2, H_2O and CO, and the line-by-line spectral database. In the flame zone, $\kappa_P \approx 0.5 \, m^{-1}$, which is relatively optically thin at a length scale of the device dimension (1 m). However, outside of the flame, κ_P is as high as $4 \, m^{-1}$, which is optically very thick. The computed mean absorption coefficient distribution shown in [20] using a WSGGM model has a similar shape, but with lower values of κ_P (0 to $0.5 \, m^{-1}$). The value of κ_P also can be estimated using the measured mean temperature, CO_2 and H_2O concentrations and the spectral database; this calculation gives $\kappa_P \approx 2 \, m^{-1}$ at the exit plane of the burner, which is close to the value shown in Figure 4.

Computed profiles of mean temperature, velocity and major species for the baseline model (including radiation) and for the same model with radiation deactivated are shown in Figure 5. The difference in computed mean temperatures is as high as 400 K, and the results obtained with radiation are in better agreement with experiment. The influence of radiation is more pronounced in the recirculation zone than in the flame zone. This is consistent with Figure 4 and the discussion there. The better temperature prediction with radiation brings the CO and CO_2 profiles closer to the experimental data. The net effect of radiation on mean composition is to shift the CO/CO_2 ratio in favour of higher CO_2 and lower CO, while the change in oxygen mole fraction is small. This is a straightforward thermodynamic effect: equilibrium of the reaction $CO_2 + H \rightleftharpoons CO + OH$ shifts in favour of CO_2 at lower temperatures. This effect is less pronounced in air–fuel combustion because of the lower CO_2 concentration and lower temperature. Similar trends have been found with all three chemical mechanisms and with both the WSR and the PDF models (not shown).

CO concentrations in oxy–fuel combustion are high compared to air–fuel combustion, and it has been suggested that CO might be important as a radiatively participating species. This is explored in Figures 6 and 7. Over the temperature range of 1000 K to 2500 K, the Planck mean absorption coefficient of CO_2 is approximately a factor of 10 higher than that of CO (Figure 6). The local mean CO_2 mole fraction is larger than the local mean CO mole fraction at most locations in the furnace, with the exception of a small area on the fuel-rich side of the flame (Figure 2). For these reasons, the net radiative contribution of CO is relatively small. This is confirmed in Figure 7, where small differences in computed mean temperature profiles (maximum difference of 30 K) are found at two axial locations with versus without consideration of CO radiation. From a computational point of view, the increase in CPU time with versus without CO as a radiatively participating species is negligible, although the spectral database size increases as more species are considered.

4.3. *Chemical kinetics*

Results obtained using three chemical mechanisms are compared in Figure 8. As discussed earlier, CO_2 is chemically active in oxy–fuel combustion, and this is a major difference between oxy–fuel and air–fuel combustion. The CO_2 activity involves interconversion with CO and consumption of free radicals including H, O and OH. This alters the O/H radical pool, which in turn can affect the fuel oxidation.

Mean temperature, CO_2, CO and O_2 profiles are similar for GRI-Mech 2.11 and for the 21-species C1 mechanism (Figure 8), and results from these two mechanisms generally are in better agreement with experiment compared to the 16-species mechanism, especially for CO_2 and O_2. At all three axial locations, the 16-species mechanism yields both lower CO and lower CO_2 compared to the other two mechanisms. The water mass fractions at the exit of the furnace predicted by the 21-species C1 mechanism and GRI-Mech 2.11 are 0.417 and 0.425, respectively. These results are closer to the experimental value (0.421 [16])
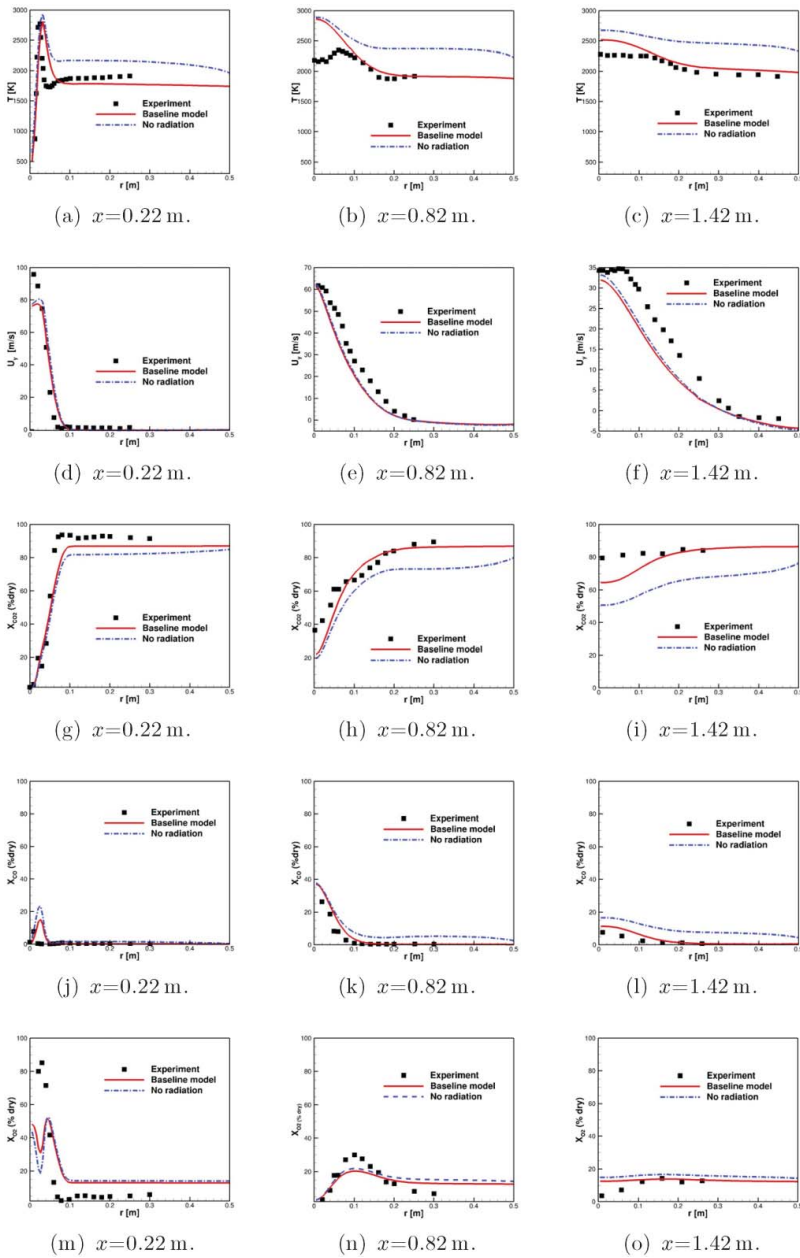
Figure 5. Computed (with versus without radiation) and measured radial profiles of mean temperature, axial velocity, CO_2, CO and O_2 (available in colour online).

compared to the prediction from the 16-species mechanism, which is 0.38. Chemical equilibrium calculations performed using the three mechanisms (or, more accurately, their corresponding thermodynamic data) show minor differences (e.g., differences in adiabatic flame temperatures are less than 5 K, and equilibrium compositions are similar). Chemical equilibrium calculations also show that the exit composition corresponds to the local
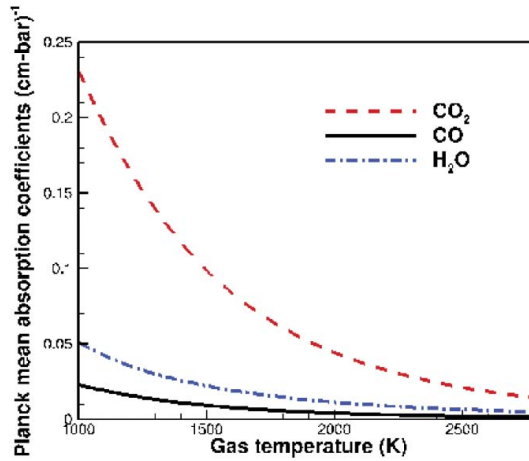
Figure 6. Pressure-based Planck mean absorption coefficients for CO, CO_2 and H_2O as functions of temperature (available in colour online).

equilibrium state for all three mechanisms. Thus, the differences in Figure 8 and in the exit compositions could be a result of the upstream finite-rate chemistry and the differences in the reaction set and rates associated with each mechanism.

The 16-species mechanism has been found to be adequate for temperature and major-species predictions in laboratory methane–air flames [35]. However, it would need to be modified for use in oxy–fuel combustion. In the 16-species mechanism, the only reaction involving CO_2 and other species is $CO_2 + H \rightleftharpoons CO + OH$. The consumption of H atoms competes with the main chain-branching reaction $H + O_2 \rightleftharpoons O + OH$, which reduces the generation of chain carriers. The simplified CO_2 chemistry in the 16-species mechanism could lead to inaccurate consumption of H atoms, which results in underprediction of CO_2 and overprediction of O_2. The other two mechanisms involve larger sets of CO_2 reactions, and they also give better results compared with experimental data.

Given similar accuracy in the prediction of the major species, the 21-species C1 mechanism has the advantage of lower computational time (approximately 60% reduction in total simulation time compared to the baseline model with the radiation model off), while GRI-Mech 2.11 has a more comprehensive set of CO_2/CO reactions.

(a) $x = 0.22$ m.

(b) $x = 1.42$ m.
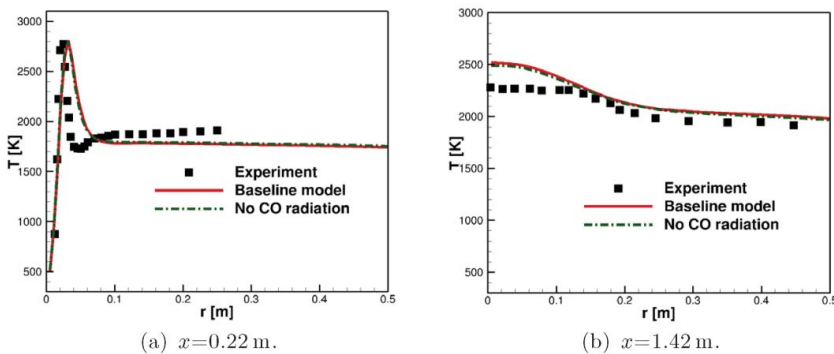
Figure 7. Computed (with versus without CO radiation) and measured radial profiles of mean temperature (available in colour online).
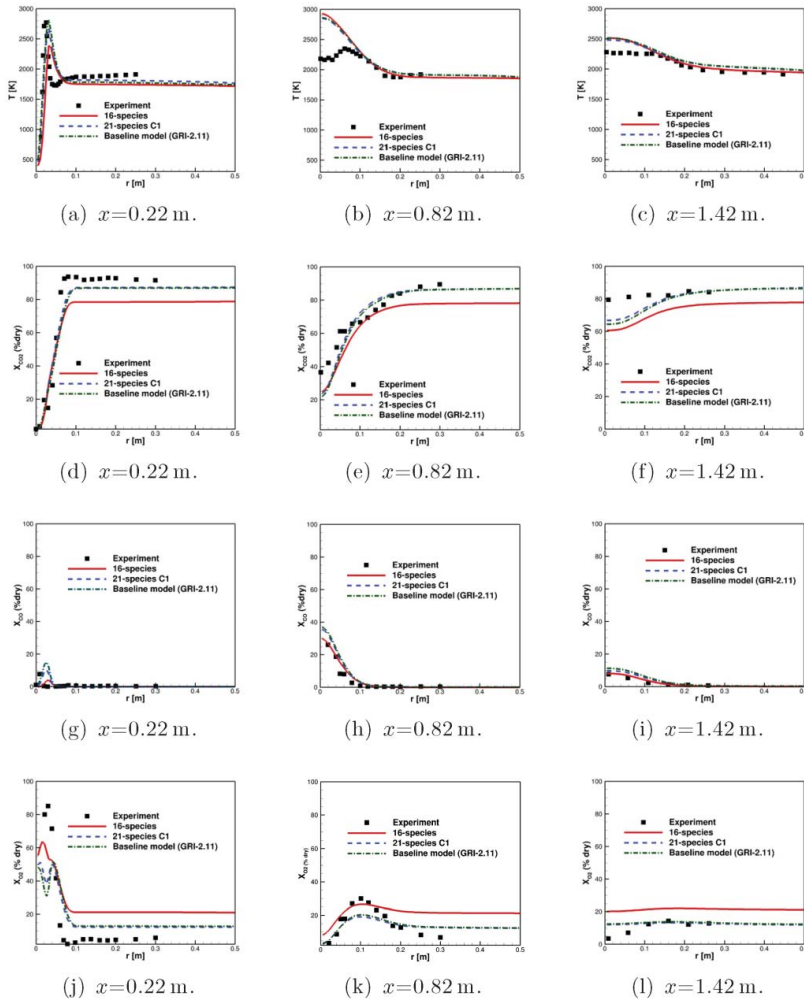
Figure 8. Computed (three chemical mechanisms) and measured radial profiles of mean temperature, CO_2, CO and O_2 (available in colour online).

4.4. *Turbulence-chemistry-radiation interactions*

The influences of turbulent fluctuations in composition and temperature on global values and flame structure are discussed next, with emphasis on interactions between turbulence, chemical kinetics and radiation heat transfer.

4.4.1. *Turbulence–chemistry interactions*

The influence of turbulent fluctuations on chemical reaction are isolated and quantified by comparing results from the PDF method with results obtained using a WSR chemistry model. To separate chemistry effects from radiation effects, the comparison is made with the radiation model off. This results in unrealistically high temperatures and correspondingly faster chemistry, and therefore will tend to understate the importance of fluctuations.
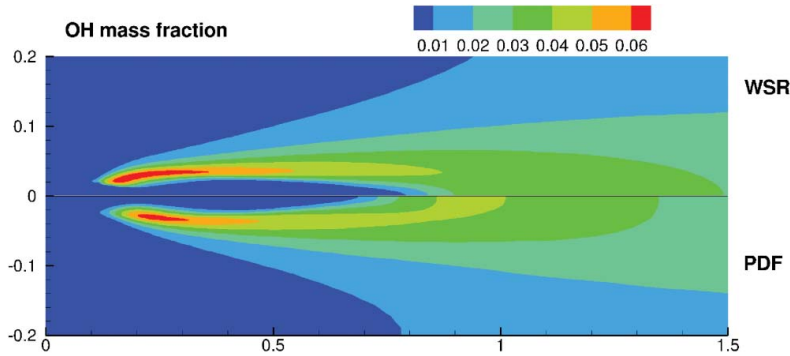
Figure 9. Computed (WSR versus PDF models, without radiation) contours of mean OH mass fraction (available in colour online).

Computed turbulent flame structures (mean OH mass fraction contours) from the two models are compared in Figure 9. Significant differences are evident, even with the unrealistically high temperatures. The PDF model gives a longer liftoff length and lower peak mean OH level compared to the WSR model. This is in keeping with observations that have been made in other PDF-based modelling studies of lifted turbulent jet flames, where it has been shown that the PDF-based turbulent flame structure is more consistent with experiment [45]. Quantitative differences in computed mean values between the two models are most evident in the CO profiles (Figure 10); the differences would be greater (and the agreement with experiment would be better) with consideration of radiation.

4.4.2. *Turbulence–radiation interactions*

The influence of turbulent fluctuations on radiation are isolated and quantified by comparing results obtained by computing radiation based on PDF particle values of composition and temperature with those obtained by computing radiation based on finite-volume cell-mean values of composition and temperature. Examples are provided in Figures 11 and 12.

Emission TRI are explored by comparing the local time-averaged mean radiative emission computed based on PDF particle values of composition and temperature, $\langle \kappa_P(T, \boldsymbol{Y})T^4 \rangle$, to the local time-averaged mean radiative emission based on finite-volume cell-mean values of composition and temperature, $\kappa_P(\langle T \rangle, \langle \boldsymbol{Y} \rangle)\langle T \rangle^4$. The total emission TRI can be decomposed into three contributions as follows, similar to what was done in [13,29] in the context of large-eddy simulation:

$$\frac{\langle \kappa_P(T, \boldsymbol{Y})T^4 \rangle}{\kappa_P(\langle T \rangle, \langle \boldsymbol{Y} \rangle)\langle T \rangle^4} = \frac{\langle \kappa_P(T, \boldsymbol{Y})T^4 \rangle}{\langle \kappa_P(T, \boldsymbol{Y}) \rangle \langle T^4 \rangle} \times \frac{\langle \kappa_P(T, \boldsymbol{Y}) \rangle}{\kappa_P(\langle T \rangle, \langle \boldsymbol{Y} \rangle)} \times \frac{\langle T^4 \rangle}{\langle T \rangle^4} \ . \tag{2}$$

Here, the left-hand side corresponds to the total emission TRI, and the three terms on the right-hand side are, respectively, the absorption coefficient–Planck function correlation ('term 1'), the absorption coefficient self-correlation ('term 2'), and the temperature self-correlation ('term 3'). Departures of any of these terms from unity are manifestations of TRI; values greater than one mean that radiative emission is enhanced by turbulent fluctuations, while values less than one mean that radiative emission is diminished by turbulent fluctuations.
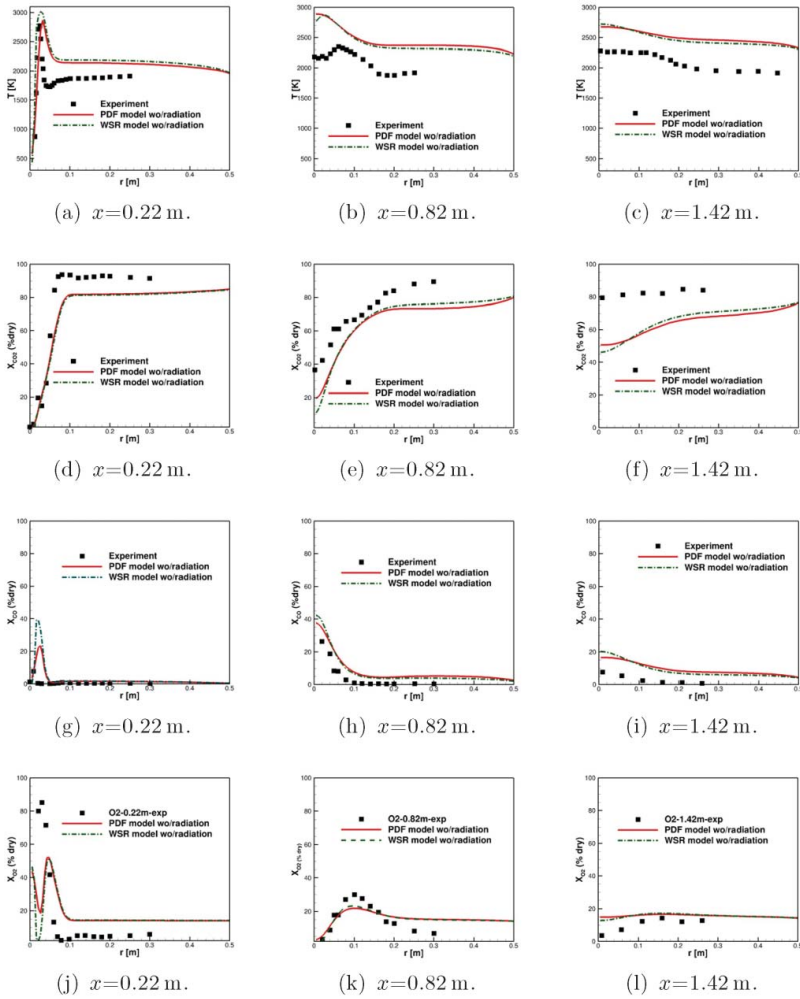
Figure 10. Computed (WSR versus PDF models, without radiation) and measured radial profiles of mean temperature, CO_2, CO and O_2 (available in colour online).
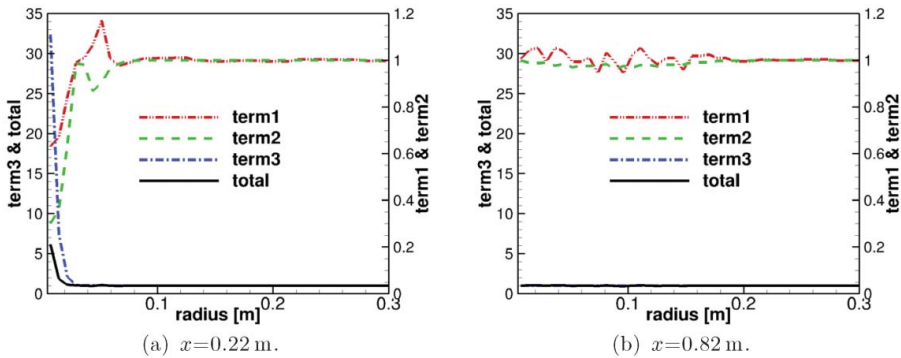
Figure 11. Computed (baseline model) radial profiles of emission TRI terms (available in colour online).

Figure 11 shows radial profiles of the emission-TRI-related variables defined in Equation (2) at two axial locations. In the flame zone (small r at $x = 0.22$ m), turbulent fluctuations are large and strong local TRI effects can be seen. The temperature self-correlation (term 3) exceeds a value of 30 at some locations. Interestingly, the absorption coefficient–Planck function correlation (term 1) and the absorption coefficient self-correlation (term 2) are both less than unity in the flame zone. This is a consequence of the opposing influences of temperature and CO_2/CO ratio on the absorption coefficient. The absorption coefficient increases with increasing ratio of CO_2/CO and decreases with increasing temperature, and the temperature and CO_2/CO ratio fluctuations are negatively correlated in the flame zone (not shown). The maximum net local enhancement of radiative emission due to TRI (total) is approximately a factor of six to seven. Outside of the flame zone, in the large recirculation zone and at downstream locations, turbulent fluctuations are small and TRI effects are correspondingly small; all emission TRI terms are close to unity there.

While strong local TRI effects are found in the flame zone, their influence on mean and rms temperature and species profiles is small. This can be seen in Figure 12, where results from two fully coupled simulations are compared. In one case, radiative emission and absorption are computed using PDF particle values (thereby accounting for both emission and absorption TRI), while in the other case, radiative emission and absorption are computed using finite-volume cell-mean values (thereby neglecting both emission and absorption TRI). In both cases, chemistry is computed based on particle values so that TCI are
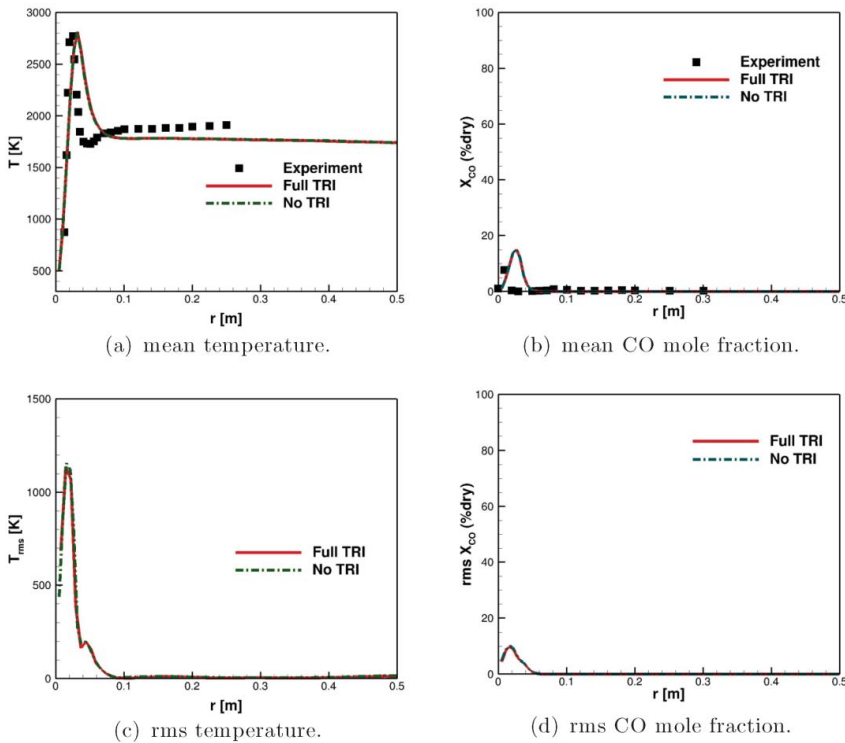
Figure 12.   Computed (with versus without TRI) and measured radial profiles of mean and rms temperature and CO mole fraction. All results are at $x = 0.22$ m (available in colour online).
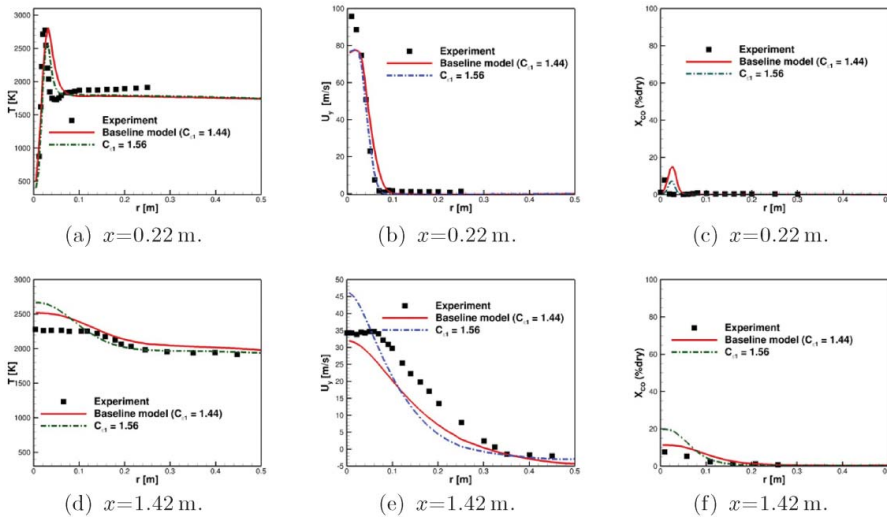
Figure 13. Computed (two values of $C_{\varepsilon 1}$) and measured radial profiles of mean temperature, velocity and CO (available in colour online).

accounted for. Differences in computed mean and rms temperatures and CO concentrations are negligible.

4.4.3. *Turbulence and mixing models*

As discussed earlier, the value of $C_{\epsilon 1}$ in the k–ε model is often increased from its standard value in modelling studies of turbulent free round jets to increase the penetration and decrease the spread rate; this has also been done in some of the earlier OXYFLAM-2A modelling studies (Table 2). The effects of increasing $C_{\epsilon 1}$ from 1.44 (the standard value) to 1.56 are shown in Figure 13. For the models that have been used here, the standard value of $C_{\epsilon 1}$ gives results that are in closer agreement with experiment.

The mixing model also plays a central role in PDF methods. Results obtained using two different mixing models (baseline EMST versus a modified Curl model [46]) were compared for the same value of C_{ϕ}, and only minor differences were found in the radial profiles of mean temperature and composition (not shown). Examples of results obtained using EMST for two values of C_{ϕ} (baseline $C_{\phi} = 5.5$ versus $C_{\phi} = 2.5$) are shown in Figures 14 and 15. The computed mean OH mass fraction contour shows a more highly lifted and less intense flame for the smaller value of $C_{\phi} = 2.5$, and the computed maximum mean temperature drops from 2974.6 K for $C_{\phi} = 5.5$ to 2895.2 K for $C_{\phi} = 2.5$. In general, reducing C_{ϕ} reduces the mixing rate and increases the magnitude of the local composition and temperature fluctuations; in the limit $C_{\phi} \to \infty$, the PDF model results approach those for a WSR chemistry model. The mean CO mole fraction profile obtained with $C_{\phi} = 2.5$ is closer to the experimental profile, while the mean temperature profile obtained with $C_{\phi} = 5.5$ is closer to experiment. Here the baseline value of C_{ϕ} was selected based primarily on matching the computed mean temperature profiles to experiment. However, given the large uncertainties in temperature measurements above 2200 K, and the limited data that are available for this flame, it cannot be said with certainty that $C_{\phi} = 5.5$ is the optimal value.

(a) Mean OH mass fraction.

(b) Mean CO mass fraction.
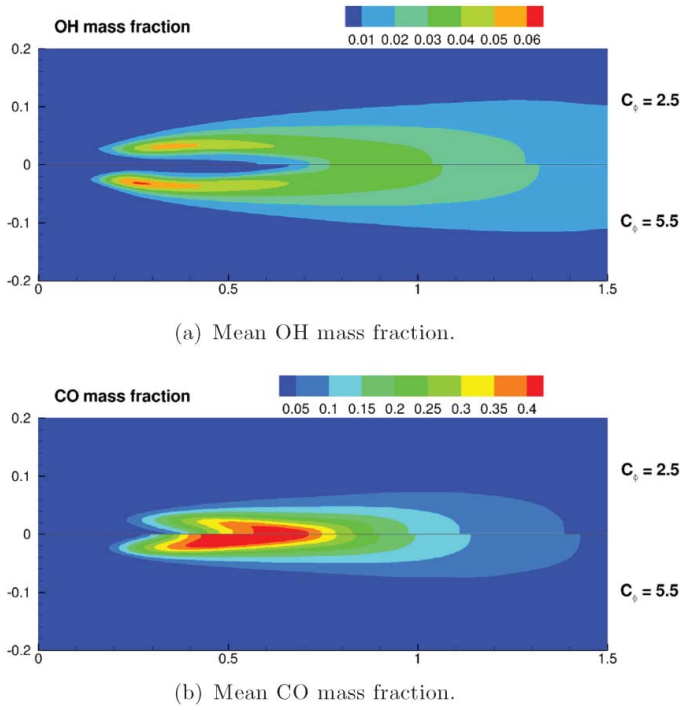
Figure 14.   Computed (two values of C_ϕ) mean OH and CO mass-fraction contours (available in colour online).

(a) Mean temperature, $x = 0.22\,\mathrm{m}$.   (b) Mean CO mole fraction, $x = 0.22\,\mathrm{m}$.
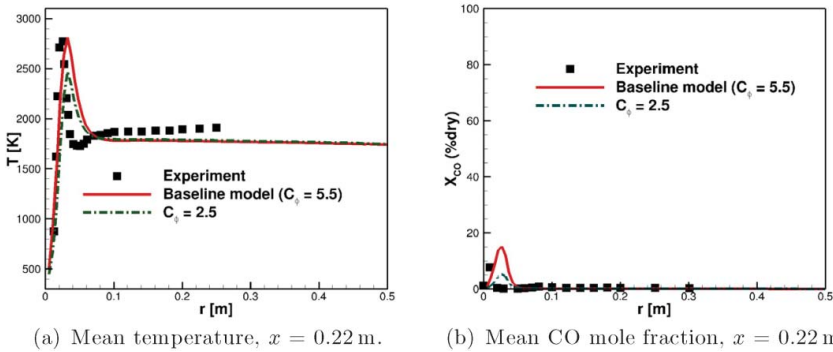
Figure 15.   Computed (two values of C_ϕ) and measured radial profiles of mean temperature and CO mole fraction (available in colour online).

5.   Conclusions

Numerical simulations have been performed for a 0.8 MW oxy–natural gas burner, and results have been compared with experimental measurements. The simulations include detailed chemistry (up to 49 species) and radiation (a photon Monte Carlo method with line-by-line spectral resolution), and a transported PDF method to account for turbulent fluctuations in composition and temperature. Compared to earlier PDF/PMC/LBL modelling studies, the spectral radiation database has been extended to include CO (in addition to CO_2 and H_2O) and temperatures up to 3000 K, and the wall radiation boundary conditions

have been expanded to account for hot walls with absorption and diffuse grey reflection and emission. The level of agreement between the model and experiment is at least as good as any that has been published earlier. Remaining discrepancies between model and experiment may be attributed, in part, to simplifications that have been made in the specification of inlet boundary conditions and the geometric configuration.

The 'high-fidelity' CFD model was then exercised to provide deeper insight into high-temperature oxy–fuel combustion, and guidance for developing simpler models. This was done by performing a series of parametric model variations to isolate and quantify the influences of gas-phase chemistry, radiation and turbulence-chemistry-radiation interactions. Salient findings are as follows. For high-temperature oxy–fuel combustion, it is essential to have accurate high-temperature thermodynamic property data and to account for dissociation. Accurate CO_2 kinetics are also important. Chemical mechanisms that account for the interconversion of CO and CO_2 (e.g., GRI-Mech 2.11) and/or that have been developed specifically for oxy–fuel combustion environments (e.g., the 21-species C1 mechanism) perform reasonably well. Radiation plays a dominant role, as expected. Neglecting radiation altogether leads to overprediction of mean temperatures by as much as 400 K through much of the furnace. The photon Monte Carlo method with line-by-line spectral resolution provides accurate estimates of the local absorption coefficient distribution in the furnace, compared to earlier work where grey models or highly simplified spectral treatments were used; this will be important for subsequent simulations of heat transfer. PMC/LBL also allows the effects of molecular gas radiation and wall radiation to be clearly separated and quantified, which will be useful for developing or choosing simpler radiation models for more routine engineering calculations. CO radiation was found to play a minor role in this burner. Radiation and chemistry are tightly coupled through the temperature, and correct temperature prediction is a prerequisite to correct prediction of the CO/CO_2 ratio. Even at the high temperatures encountered in this device, turbulence–chemistry interactions influence the computed flame structure and mean CO levels. Strong local effects of turbulence–radiation interactions are found in the flame, but the net influence of TRI on computed mean temperature and species profiles is small. This is because outside of the relatively compact turbulent flame, the temperature and composition fluctuations are small.

As we move towards simulations of realistic high-temperature oxy–coal combustors, the combustion environment will become even less amenable to making reliable experimental measurements. Therefore, in spite of the considerable modelling uncertainties, high-fidelity CFD tools such as the ones that are being developed here will increasingly be relied on to provide guidance for combustion-system development. Accurate treatment of radiation will become even more important because of the presence of high-temperature coal particles and soot, and the elevated operating pressures. And turbulence–chemistry interactions will play an important role in emissions chemistry, in particular, including NO_x from fuel-bound nitrogen.

implied, or assumes any legal liability or responsibility for the accuracy, completeness, or usefulness of any information, apparatus, product, or process disclosed, or represents that its use would not infringe privately owned rights. Reference herein to any specific commercial product, process, or service by trade name, trademark, manufacturer, or otherwise, does not necessarily constitute or imply its endorsement, recommendation, or favouring by the United States Government or any agency thereof. The views and opinions of authors expressed herein do not necessarily state or reflect those of the United States Government or any agency thereof.

References

[1] IEA, *CO$_2$ emissions from fuel combustion highlights*, 2011 ed. Available at www.iea.org/co2highlights/CO2highlights.pdf.

[2] L. Chen, S.Z. Yong, and A.F. Ghoniem, *Oxy–fuel combustion of pulverized coal: Characterization, fundamentals, stabilization and CFD modeling*, Prog. Energy Combust. Sci. 38 (2012), pp. 156–214.

[3] N. Kayukawa, *Open-cycle magnetohydrodynamic electrical power generation: A review and future perspectives*, Prog. Energy Combust. Sci. 30 (2004), pp. 33–60.

[4] C.R. Woodside, K.H. Casleton, J. Pepper, I.B. Celik, D.C. Haworth, E.D. Huckaby, O.A. Marzouk, T. Ochs, D. Oryshchyn, G. Richards, P.A. Strakey, J. Escobar-Vargas, and X.Y. Zhao, *Direct power extraction with oxy-combustion: An overview of magnetohydrodynamic research activities at the NETL-RUA*, in *2012 International Pittsburgh Coal Conference*, 15–18 October 2012, Pittsburgh, PA, 2012.

[5] C.E. Baukal Jr (ed.), *Oxygen-Enhanced Combustion*, CRC Press, Boca Raton, FL, 1998.

[6] P. Edge, M. Gharebaghi, R. Irons, R. Porter, R.T.J. Porter, M. Pourkashanian, D. Smith, P. Stephenson, and A. Williams, *Combustion modelling opportunities and challenges for oxy–coal carbon capture technology*, Chem. Eng. Res. Des. 89 (2011), pp. 1470–1493.

[7] A. Wang and M.F. Modest, *Spectral Monte Carlo models for nongray radiation analyses in inhomogeneous participating media*, Int. J. Heat Mass Transfer 50 (2007), pp. 3877–3889.

[8] S.B. Pope, *PDF methods for turbulent reactive flows*, Prog. Energy Combust. Sci. 11 (1985), pp. 119–192.

[9] D.C. Haworth, *Progress in probability density function methods for turbulent reacting flows*, Prog. Energy Combust. Sci. 36 (2010), pp. 168–259.

[10] D.C. Haworth and S.B. Pope, *Transported probability density function methods for Reynolds-averaged and large-eddy simulations*, in *Turbulent Combustion Modeling – Advances, New Trends and Perspectives*, T. Echekki and E. Mastorakos, eds., Springer, 2011, pp. 119–142.

[11] R.S. Mehta, D.C. Haworth, and M.F. Modest, *Composition PDF/photon Monte Carlo modeling of moderately sooting turbulent jet flames*, Combust. Flame 157 (2010), pp. 982–994.

[12] R.S. Mehta, M.F. Modest, and D.C. Haworth, *Radiation characteristics and turbulence–radiation interactions in sooting turbulent jet flames*, Combust. Theory Modell. 14 (2010), pp. 105–124.

[13] A. Gupta, D.C. Haworth, and M.F. Modest, *Turbulence–radiation interactions in large-eddy simulations of luminous and nonluminous nonpremixed flames*, Proc. Combust. Inst. 34 (2013), pp. 1281–1288.

[14] R.S. Barlow, G.J. Fiechtner, C.D. Carter, and J.Y. Chen, *Experiments on the scalar structure of turbulent CO/H$_2$/N$_2$ jet flames*, Combust. Flame 120 (2000), pp. 549–569.

[15] X.Y. Zhao, D.C. Haworth, and E.D. Huckaby, *Transported PDF modeling of nonpremixed turbulent CO/H$_2$/N$_2$ jet flames*, Combust. Sci. Technol. 184 (2012), pp. 676–693.

[16] N. Lallemant, F. Breussin, R. Weber, T. Ekman, J. Dugue, J.M. Samaniego, O. Charon, A.J.V.D. Hoogen, J.V.D. Bemt, W. Fujisaki, T. Imanari, T. Nakamura, and K. Iino, *Flame structure, heat transfer and pollutant emissions characteristics of oxy–natural gas flames in the 0.7-1 MW thermal input range*, J. Inst. Energy 73 (2000), pp. 169–182.

[17] N. Lallemant, J. Dugue, and R. Weber, *Measurement techniques for studying oxy–natural gas flames*, J. Inst. Energy 76 (2003), pp. 38–53.

[18] C.K. Westbrook and F.L. Dryer, *Simplified reaction mechanisms for the oxidation of hydrocarbon fuels in flames*, Combust. Sci. Technol. 27 (1981), pp. 31–43.

[19] W.P. Jones and R.P. Lindstedt, *Global reaction schemes for hydrocarbon combustion*, Combust. Flame 73 (1988), pp. 233–249.

[20] C. Yin, L.A. Rosendahl, and S.K. Kær, *Chemistry and radiation in oxy–fuel combustion: A computational fluid dynamics modeling study*, Fuel 90 (2011), pp. 2519–2529.

[21] A. Frassoldati, A. Cuoci, T. Faravelli, E. Ranzi, C. Candusso, and D. Tolazzi, *Simplified kinetic schemes for oxy–fuel combustion*, in *1st International Conference on Sustainable Fossil Fuels for Future Energy*, 6–10 July 2009, Rome, 2009.

[22] T. Poinsot and D. Veynante, *Theoretical and Numerical Combustion*, 3rd ed., Poinsot & Veynante, Toulouse, France, 2012. Available at http://elearning.cerfacs.fr/combustion/onlinePoinsotBook/buythirdedition/index.php.

[23] F. Breussin, N. Lallemant, and R. Weber, *Computing of oxy–natural gas flames using both a global combustion scheme and a chemical equilibrium procedure*, Combust. Sci. Technol. 160 (2000), pp. 369–397.

[24] A. Brink, M. Hupa, F. Breussin, N. Lallemant, and R. Weber, *Modeling of oxy–natural gas combustion chemistry*, J. Propulsion & Power 16 (2000), pp. 609–614.

[25] G. Kim and Y. Kim, *Non-adiabatic flamelet modeling for combustion processes of oxy–natural gas flame*, J. Mech. Sci. Technol. 19 (2005), pp. 1781–1789.

[26] G. Kim, Y. Kim, and Y.J. Joo, *Conditional moment closure for modeling combustion processes and structure of oxy–natural gas flame*, Energy Fuels 23 (2009), pp. 4370–4377.

[27] A. Wang and M.F. Modest, *Photon Monte Carlo simulation for radiative transfer in gaseous media represented by discrete particle fields*, J. Heat Transfer 128 (2006), pp. 1041–1049.

[28] A. Wang and M.F. Modest, *An adaptive emission model for Monte Carlo simulations in highly inhomogeneous media represented by stochastic particle fields*, J. Quant. Spectrosc. Radiat. Transfer 104 (2007), pp. 288–296.

[29] A. Gupta, *Large-eddy simulation of turbulent flames with radiation heat transfer*, Ph.D. diss., Pennsylvania State University, University Park, PA, 2011.

[30] P. Glarborg and L. Bentzen, *Chemical effects of a high CO_2 concentration in oxy–fuel combustion of methane*, Energy Fuels 22 (2008), pp. 291–296.

[31] F. Liu, H. Guo, and G.J. Smallwood, *The chemical effect of CO_2 replacement of N_2 in air on the burning velocity of CH_4 and H_2 premixed flames*, Combust. Flame 133 (2003), pp. 495–497.

[32] C.T. Bowman, R.K. Hanson, D.F. Davidson, W.C. Gardiner, V. Lissianski, G.P. Smith, D.M. Golden, M. Frenklach, and M. Goldenberg, GRI-Mech 2.11, 1995. Available at http://www.me.berkeley.edu/gri_mech.

[33] J. Li, Z. Zhao, A. Kazakov, M. Chaos, F.L. Dryer, and J.J. Scire Jr, *A comprehensive kinetic mechanism for CO, CH_2O, CH_3OH combustion*, Int. J. Chem. Kinet. 39 (2007), pp. 109–136.

[34] S. James, M.S. Anand, M.K. Razdan, and S.B. Pope, *In situ detailed chemistry calculations in combustor flow analyses*, J. Eng. Gas Turbines Power 123 (2001), pp. 747–756.

[35] J. Jaishree and D.C. Haworth, *Comparisons of Lagrangian and Eulerian PDF methods in simulations of nonpremixed turbulent jet flames with moderate-to-strong turbulence–chemistry interactions*, Combust. Theory Modell. 16 (2012), pp. 435–463.

[36] S. Subramaniam and S.B. Pope, *A mixing model for turbulent reactive flows based on Euclidean minimum spanning trees*, Combust. Flame 115 (1998), pp. 487–514.

[37] *OpenFOAM: The open source CFD toolbox*. Available at http://www.openfoam.org.

[38] M. Muradoglu, P. Jenny, S.B. Pope, and D.A. Caughey, *A consistent hybrid finite volume/particle method for the PDF equations of turbulent reactive flows*, J. Comput. Phys. 154 (1999), pp. 342–371.

[39] M. Muradoglu, S.B. Pope, and D.A. Caughey, *The hybrid method for the PDF equations of turbulent reactive flows: Consistency conditions and correction algorithms*, J. Comput. Phys. 172 (2001), pp. 841–878.

[40] M.F. Modest, *Radiative Heat Transfer*, 2nd ed., Academic Press, 2003.

[41] A. Wang and M.F. Modest, *Importance of combined Lorentz–Doppler broadening in high-temperature radiative heat transfer applications*, J. Heat Transfer 126 (2004), pp. 858–861.

[42] L.S. Rothman, I.E. Gordon, R.J. Barber, H. Dothe, R.R. Gamache, A. Goldman, V.I. Perevalov, S.A. Tashkun, and J. Tennyson, *HITEMP, the high-temperature molecular spectroscopic database*, J. Quant. Spectrosc. Radiat. Transfer 111 (2010), pp. 2139–2150.

[43] A. Saljnikov, M. Komatina, V. Manovic, M. Gojak, and D. Goricanec, *Investigation on thermal radiation spectra of coal ash deposits*, Int. J. Heat Mass Transfer 52 (2009), pp. 2871–2884.

[44] L. Lu and S.B. Pope, *An improved algorithm for* in situ *adaptive tabulation*, J. Comput. Phys. 228 (2009), pp. 361–386.

[45] S. Bhattacharjee, *PDF modeling of high-pressure turbulent spray combustion under diesel-engine-like conditions*, Ph.D. diss., Pennsylvania State University, University Park, PA, 2012.

[46] R.L. Curl, *Dispersed phase mixing. I. Theory and effects in simple reactors*, AIChE J. 9 (1963), pp. 175–181.